Title

Enhanced valley splitting of WSe2 in twisted van der Waals WSe2/CrI3 heterostructures

Journal

npj Computational Materials, 8(1)

ISSN

2057-3960

Authors

Ge, Mei
Wang, Han
Wu, Jizheng
et al.

Publication Date

2022

DOI

10.1038/s41524-022-00715-9

Peer reviewed

npj | Computational Materials

www.nature.com/npjcompumats

ARTICLE OPEN

Enhanced valley splitting of WSe_2 in twisted van der Waals WSe_2/CrI_3 heterostructures

Mei Ge[1], Han Wang[2], Jizheng Wu[3], Chen Si[3], Junfeng Zhang[1]✉ and Shengbai Zhang[4]✉

Van der Waals (vdW) heterostructures composed of different two-dimensional (2D) materials offer an easily accessible way to combine properties of individual materials for applications. Owing to the discovery of a set of unanticipated physical phenomena, the twisted 2D vdW heterostructures have gained considerable attention recently. Here, we report enhanced valley splitting in twisted 2D vdW WSe_2/CrI_3 heterostructures. In particular, the splitting can be 1200% (or 5.18 meV) of the value for a non-twisted heterostructure. According to the $k{\cdot}p$ model, this value is equivalent to a ~20 T external magnetic field applied perpendicular to the 2D sheet. The thermodynamic stability of 2D vdW WSe_2/CrI_3 heterostructures, on the other hand, depends linearly on the interlayer twisting angle.

npj Computational Materials (2022)8:32 ; https://doi.org/10.1038/s41524-022-00715-9

INTRODUCTION

Since the discovery of graphene[1], some other atomically thin 2D materials, such as transition metal dichalcogenides (TMDs)[2–6] and 2D magnetic chromium triiodide (CrI_3)[7,8], have gained attention because of their fascinating properties for applications. As a matter of fact, TMDs have a long historical standing as semiconductors with layered structures[9]. Early in 2010, Mak et al.[5] and Splendiani et al.[3] have revealed independently, that a strong photoluminescence emerges when MoS_2 crystal is thinned down to a monolayer, indicating an indirect to direct bandgap transition. Henceforth, there is a strong resurgence of interest in 2D TMDs, owing to the challenges and opportunities for applications in electronics[10], optoelectronics[11], and spintronics[2,12,13].

Beyond individual materials, stacking different 2D materials into vdW heterostructures can give us more room to achieve improved functions[14,15]. Except for AA or AB stacking, 2D vdW twisted heterostructures[16], in which one layer is rotated with respect to the other by an angle θ, are also interesting owing to their unexpectedly physical properties. For instance, Cao et al.[17] reported unconventional superconductivity emerging in 2D twisted bilayer graphene, and Wu et al.[18] showed topological insulators in 2D twisted TMDs homostructures. Similarly, Liao et al.[19] experimentally confirmed a ~5 times enhancement of vertical conductivity in twisted MoS_2/graphene heterostructures. These emerging twistronics merging spintronics could pave the way for future 2D material design and applications[20].

In monolayer TMDs, a pair of degenerate but inequivalent energy valleys (K, K′) in momentum space, protected by time-reversal symmetry, become the third degree of freedom for information storage, other than charge and electron spin[21]. To break the time-reversal symmetry, one of the effective approaches is applying an external perpendicular magnetic field (**B**) on TMDs, which can induce valley polarization through the Zeeman effect. Li et al.[22] obtained the magnitude of valley splitting of 0.12 meV T^{-1} in monolayer $MoSe_2$, with **B** ranging from −10 to 10 T. Similarly, in monolayer WSe_2, the valley splitting up to 0.25 meV T^{-1} is obtained[23,24]. However, a large external magnetic field is impractical for devices. Therefore, incorporating intrinsic 2D magnetic materials into vdW heterostructures, utilizing the large magnetic proximity effect (MPE), is an attractive alternative. It has been shown that MPE originating from 2D substrate can enhance the valley splitting[25,26].

The recently fabricated magnetic monolayer CrI_3[7,27] with an out-of-plane easy axis is a suitable candidate to generate MPE when forming 2D vdW heterostructures with TMDs[28]. Zhong et al.[29] experimentally demonstrated that up to 3.5 meV valley splitting (which is equivalent to ~10 T external **B** in single-layer WSe_2) has been achieved. Furthermore, this MPE can be tuned optically, which in turn alters the valley splitting of WSe_2[30]. Theoretical investigations also demonstrated that the valley degeneracy of WSe_2 can be lifted in a vdW WSe_2/CrI_3 heterostructure because the time-reversal symmetry is broken by magnetic Cr ions[31–33]. Zhang et al.[31] showed a modulated energy splitting from 0.31 to 1.04 meV, which is determined by interlayer distance and/or atom arrangement. Hu et al.[32] confirmed that the valley splitting is sensitive to interlayer distance, increasing from 2.0 to 4.5 meV when the distance was decreased by 0.3 Å from its equilibrium value. In other words, in TMD/CrI_3 heterostructures, MPE is sensitive to interlayer vdW interaction. So far, however, the role θ played in 2D vdW WSe_2/CrI_3 heterostructures is still unclear. How does the valley splitting depends on θ needs to be clarified.

In this work, we investigate a set of 2D vdW WSe_2/CrI_3 heterostructures with different θ and stacking patterns with an emphasis on the magnetic properties, such as the magnetic moment and magnetic anisotropy energy (MAE). After that, we studied the electronic properties of 2D vdW WSe_2/CrI_3 heterostructures by using a band unfolding method. The enhanced KK′ valley splitting of WSe_2, having strong dependence on θ, is obtained. Finally, we analyzed the MPE effects through the difference of partial charge density, and deduced the equivalent **B** by a $k{\cdot}p$ model[34].

RESULTS

Structural models and stability

Pristine WSe_2 has a (hexagonal) sandwiched structure, in which one W layer is sandwiched between two S layers. Pristine CrI_3 also has a sandwiched structure, with Cr layer being sandwiched

---

[1]School of Physics and Information Engineering, Shanxi Normal University, Taiyuan, China. [2]Chemical Sciences Division, Lawrence Berkeley National Laboratory, Berkeley, CA, USA. [3]School of Materials Science and Engineering, Beihang University, Beijing, China. [4]Department of Physics, Applied Physics, and Astronomy, Rensselaer Polytechnic Institute, Troy, NY, USA. ✉email: zhangjf@sxnu.edu.cn; zhangs9@rpi.edu

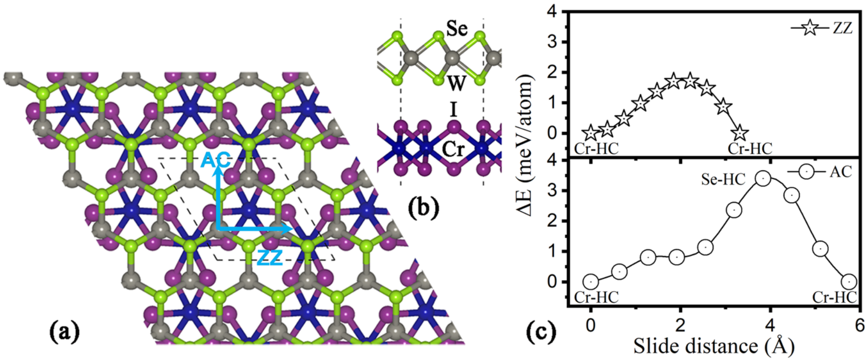

Fig. 1 Structural model and stability of non-twisted WSe_2/CrI_3 heterostructure. **a** Top and **b** side views of 2D WSe_2/CrI_3 with $\theta = 0^\circ$. Dashed lines indicate the unit cell. Blue arrows in panel **a** indicate sliding directions. **c** Energy as a function of sliding the WSe_2 with respect to CrI_3, along the ZZ and AC directions, respectively.

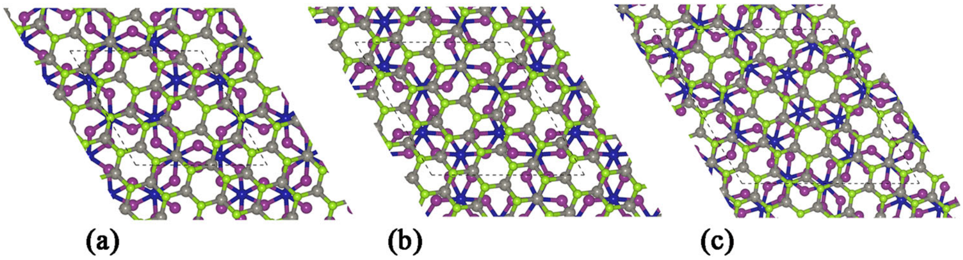

Fig. 2 Structure models of twisted WSe_2/CrI_3 heterostructures. **a** $\theta = 16.1$, **b** $\theta = 23.4$, and **c** $\theta = 28.1^\circ$.

Table 1. Structural information and properties of WSe_2/CrI_3 heterostructures for Cr-HC and Se-HC (bracket) configurations.

Adopted lattice	Twist angle (°)	Lattice constant (Å)	Lattice mismatch (%)	Interlayer distance (Å)	Formation energy (meV Å^{-2})	MAE (meVCr^{-1})	Valley splitting (meV)
WSe_2	0	6.642	−5.14	3.53 (3.56)	37.19 (36.02)	−0.93 (−0.96)	−0.43 (−0.27)
	16.1	12	−1.06	3.58 (3.59)	44.91 (44.85)	−0.57 (-0.56)	1.64 (1.74)
	23.4	14.475	3.36	3.51 (3.57)	44.68 (40.00)	−0.34 (-0.38)	5.18 (2.07)
	28.1	18.526	0.0	3.51 (3.50)	45.02 (45.05)	−0.48 (-0.49)	3.69 (3.61)
CrI_3	0	7.002	5.4	3.47 (3.67)	19.13 (17.66)	−0.54 (-0.54)	—
	16.1	12.128	1.07	3.56 (3.56)	19.30 (19.22)	−0.51 (0.27)	1.97 (0)
	23.4	14.004	−3.25	3.55 (3.56)	21.32 (21.31)	−0.76 (-0.50)	—
	28.1	18.526	0.19	3.51 (3.50)	25.23 (25.26)	−0.48 (-0.49)	3.69 (3.61)

between two I layers. We obtain the vdW WSe_2/CrI_3 heterostructure by placing a WSe_2 layer on a CrI_3 sheet, with θ ranging between 0 and 30°. To find stable configurations, we slide the WSe_2 layer relative to the CrI_3 layer. Figure 1a, b shows an example of the atomic structures with a 0° twist angle. Here, we use ten points within a unit cell along with the zigzag (ZZ) and armchair (AC) directions, respectively. Figure 1c shows the energies along with the ZZ (upper) and AC (lower) directions, both suggesting that the starting structure is most stable. Here, the Cr atom is at the hexagonal center (HC) of WSe_2, named Cr-HC hereinafter. In the following, we consider mainly the Cr-HC configurations for twisted WSe_2/CrI_3. However, we also consider other configurations, in particular, the less-stable Se-HC configurations where the Se atom is at the HC of Cr layer. The WSe_2 (CrI_3) monolayer belongs to the space group of P-6m2 (P-31m), which is reduced to P3 after stacking into the twisted heterostructures for either Cr-HC or Se-HC. The detailed atomic structures for the twisted Cr-HC structures can be found in the Supplementary Information.

For twisting, there are, in principle, many possibilities. Owing to the lattice constant difference (3.321 Å of WSe_2 *vs* 7.002 Å of CrI_3), most of them will result in huge supercells, making DFT calculations impossible. The lattice constant mismatch (δ) is defined as

$$\delta = \left(a^H - a^M\right)/a^M \times 100\% \quad (1)$$

in which a^H and a^M are the lattice constants of the heterostructure and WSe_2 (or CrI_3) monolayer, respectively. Here, we select heterostructures with a mismatch threshold of 5.5% and have considered supercells up to 20 Å in lateral size. This leads to four heterostructures with $\theta = 0$, 16.1, 23.4, and 28.1° (see Figs. 1 and 2). Detailed supercell parameters for the WSe_2/CrI_3 heterostructures are $2\times2/1\times1$ ($\theta = 0^\circ$), $\sqrt{13}\times\sqrt{13}/\sqrt{3}\times\sqrt{3}$ ($\theta = 16.1^\circ$), $\sqrt{19}\times\sqrt{19}/2\times2$ ($\theta = 23.4^\circ$), and $\sqrt{31}\times\sqrt{31}/\sqrt{7}\times\sqrt{7}$ ($\theta = 28.1^\circ$). Details for the heterostructures are given in Table 1. It should be noted that both electronic structure of WSe_2[35] and magnetic properties of CrI_3[36] are sensitive to the lattice constant. For this reason, in this work we mainly have performed two limited sets of calculations: first using the lattice parameter of WSe_2 and second using that of CrI_3 for the heterostructure. Furthermore, we investigated the strain effects on the thermodynamic stability and electronic properties for the heterostructures with the relaxed lattice parameter.

The stability of WSe_2/CrI_3 is determined by their formation energy defined as

$$E_f(\mathrm{meV\AA}^{-2}) = (E_{\mathrm{CrI3}} + E_{\mathrm{WSe2}} - E_{\mathrm{CrI3/WSe2}})/S \tag{2}$$

where S is the cross-section of the supercell, E_{CrI3}, E_{WSe2}, and $E_{\mathrm{CrI3/WSe2}}$ are total energies of respective systems. Table 1 below and Supplementary Fig. 1 show that twisted WSe_2/CrI_3 have larger E_f than that of non-twisted ones, indicating that the twisted heterostructures are more stable. Noteworthy, by using the same lattice parameters for individual and heterostructure systems, the strain energy owing to lattice mismatch have been excluded here. The energy differences between the Cr-HC and Se-HC configurations with the same twist angle θ range between 0.01 and 4.68 meV Å^{-2}, showing a high lubricity of 2D WSe_2/CrI_3 similar to that of layered graphene[37]. Also noted is that the spin-orbit coupling (SOC) part of the formation energy also depends on θ. Taking the Cr-HC with WSe_2 lattice constant as an example, we obtain $E_{f\_SOC} = 0.37$ (0°), 0.67 (16.1°), 0.61 (23.4°), and 0.75 (28.1°) meV Å^{-2}, which is in line with the trend observed for E_f.

Magnetic properties and valley splitting

Table 1 also lists the magnetic anisotropy energies (MAE), defined as the energy difference between out-of-plane ($E_\perp$) and in-plane ($E_{//}$) easy-axis per Cr atom, i.e.,

$$\mathrm{MAE} = (E_\perp - E_{//})/N_{Cr} \tag{3}$$

For WSe_2/CrI_3 with WSe_2 lattice constant, MAE decreases with increasing δ (from −5.14% of compressive strain to 3.36% of tensile strain), which is similar to monolayer CrI_3[38], but it is independent of sliding between WSe_2 and CrI_3. For WSe_2/CrI_3 with a CrI_3 lattice constant, on the other hand, only a slight fluctuation of MAE is observed.

Next, we consider the valley splitting, schematically shown in Fig. 3. With SOC, both the (high-lying) valence band (VB) and (low-lying) conduction band (CB) of WSe_2 split into two subbands: one spin up and one spin down. In particular, the VB (CB) in the K valley will split into VB1 and VB2 (CB1 and CB2) and the VB′ (CB′) in the K′ valley will split into VB1′ and VB2′ (CB1′ and CB2′), denoted by dashed lines in Fig. 3b. When WSe_2 is put on a magnetic CrI_3 substrate, the spin-up bands (red) are shifted downward and the spin-down bands (blue) are shifted upward. The VB (CB) at K and K′ with different spins will split by Δ_{VB} (Δ_{CB}), shown in Fig. 3b.

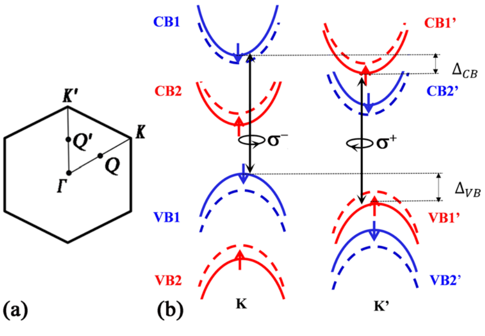

Fig. 3 Schematic diagrams of irreducible Brillouin zone and split of degeneracy at the KK′ valleys of WSe_2. a Irreducible Brillouin zone of WSe_2. **b** Split of degeneracy at the KK′ valleys. In (**b**), σ^+ and σ^-denote the right-hand and left-hand circularly polarized light under optical selection rules at the KK′ valleys. The dashed lines denote the $\mathbf{B} = 0$ bands. Red and blue arrows denote spin up and spin down states, respectively. CB1 (CB2) and VB1 (VB2) denote the first (second) conduction and valence bands at the K valley, while CB1′ (CB2′) and VB1′ (VB2′) denote the corresponding bands at the K′ valley. Δ_{CB} and Δ_{VB} are the energy shifts of the conduction and valence band, respectively.

The effective KK′ valley splitting ($\Delta_{KK'}$) is defined as

$$\Delta_{KK'} = \Delta_{CB} - \Delta_{VB} \tag{4}$$

Note that to calculate the KK′ splitting, requires the calculation of energy levels at K (K′) in the unfolded Brillouin zone. This is done as follows: the wavefunction of the supercell (Ψ) can be mapped on to those of the primitive cell ($\Psi_{\mathbf{k}}$)[39–41] by

$$\Psi_{\mathbf{k}} = \frac{1}{N}\sum\nolimits_R \chi_{\mathbf{k}}^*(\mathbf{R})\hat{T}_{\mathbf{R}}\Psi \tag{5}$$

where N is the number of primitive cells contained in the supercell, $\mathbf{k}$ is the reduced wave vector inside the first Brillouin zone,

$$\mathbf{R} = \sum_j n_j a_j \tag{6}$$

is the integral multiple of lattice vectors $\boldsymbol{a}_j$, $\hat{T}_{\mathbf{R}}$ is the translational operator for a translation $\mathbf{R}$, and

$$\chi_{\mathbf{k}}(\mathbf{R}) = e^{i\mathbf{k}\cdot\mathbf{R}} \tag{7}$$

For a given region in WSe_2/CrI_3 such as WSe_2 layer in the heterostructure, the relative weight (ρ) of layer projection in the range between Z_1 and Z_2 is given by

$$\rho = \int_{Z_1}^{Z_2} \Psi_{\mathbf{k}}^*\Psi_{\mathbf{k}} dr \tag{8}$$

as proposed by Chen and Weinert[42]. Figure 4 shows, for WSe_2/CrI_3 with WSe_2 lattice parameter, the band structures for $\theta = 0°$ and 16.1°, (a, c) before and (b, d) after band unfolding. We see that although there is interaction between WSe_2 and CrI_3, the unfolded band structures of WSe_2 look similar with a band gap of 1.24 ± 0.01 eV, close to that of monolayer WSe_2.

Table 2 lists the components for valley splitting in WSe_2. For monolayer WSe_2, both Δ_{VB} (Δ_{CB}) and $\Delta_{KK'}$ are zero due to time reversal symmetry. When placed on CrI_3, this symmetry is broken so valley splitting is generally observed. Consistent with previous calculations[31,32], at $\theta = 0°$, $|\Delta_{KK'}| = 0.43$ and 0.27 meV for Cr-HC and Se-HC, respectively. We find the enhanced valley splitting of twisted heterostructures, for either Cr-HC or Se-HC. Compared with $\theta = 0°$, the magnitude can also be magnitude larger (e.g., 0.43 meV *vs* 5.18 meV). With the parameter relaxation, as presented in Supplementary Table 1, the valley splitting of twisted WSe_2/CrI_3 heterostructure with Cr-HC is still larger than that of the non-twisted ones. We notice that the valley splitting without the twisting arises mainly from CB states, while for twisted ones, VB states also play an important role.

The enhanced valley splitting in heterostructures may be understood in terms of an MPE. This can be seen in Table 2, which shows that for both K and K′, E_{VB} decreases, but E_{CB} is nearly a constant, with an increasing θ. One may note that both the VB and CB states of WSe_2 are made of predominantly W *d* orbitals: $d_{x^2-y^2/xy}$ for VB, and d_{z^2} for CB. Figure 5a–d shows the differences in the partial charge density $\Delta\rho$ of the valence band maximum (VBM) states at K and K′. An obvious θ-dependence of $\Delta\rho$ is observed near Cr atoms. Figure 5e shows the planar averaged $\Delta\rho$ along z, $\overline{\Delta\rho}(z)$. It reveals how the states of WSe_2 is affected by the proximity of Cr atoms inside CrI_3. This analysis suggests that the VBM states are responsible for the enhanced valley splitting. Indeed, results in Table 2 support such a conclusion as it shows that valley splitting is mainly a result of a θ-dependent Δ_{VB}.

Figure 5f plots the sum of $\Delta\rho$ of Cr layer ($\Sigma\Delta\rho$) as a function of $\Delta_{KK'}$. A nearly linear dependence is observed. Since $\Delta\rho$ is a measure of proximity effect, Fig. 5f thus suggests that MPE is the reason for enhanced $\Delta_{KK'}$. Figure 5f also shows that with an increase in valley splitting, the total magnetic moment of Cr also increases from 3.011 to 3.204 μ_B. Hence, the enhanced magnetic

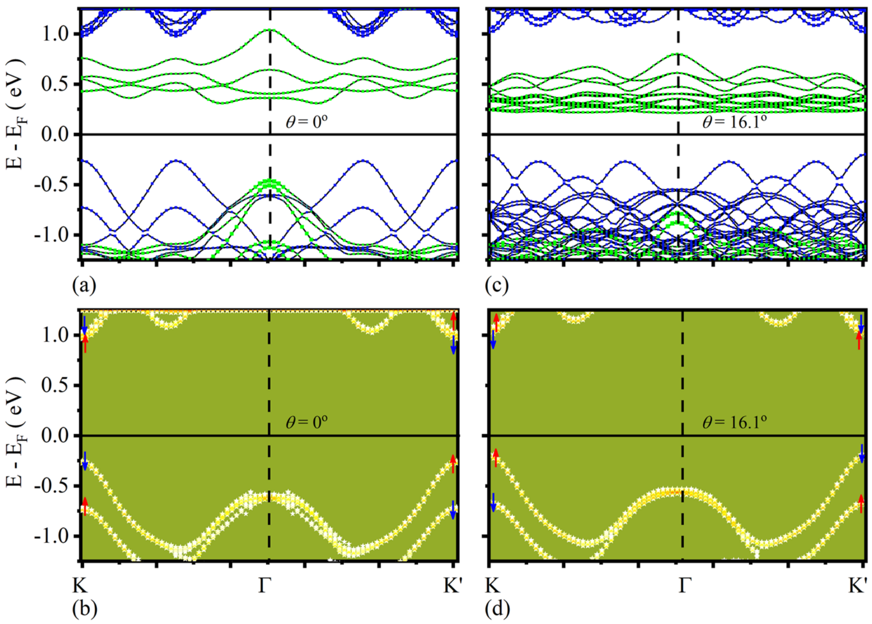

Fig. 4 Band structures of WSe_2/CrI_3 heterostructures. a, **c** are the projected ones, in which green and blue denote CrI_3 and WSe_2 states, respectively. **b**, **d** are the unfolded ones for WSe_2, in which red and blue arrows denote spin up and down states.

Table 2. Band splitting in WSe_2 and WSe_2/CrI_3 heterostructures for Cr-HC and Se-HC (bracket) configurations with WSe_2 lattice constant.

Adopted lattice	Twist angle (°)	CB shifting E_{CBK} (meV)	VB shifting E_{VBK}(meV)	CB splitting Δ_{CB} (meV)	VB splitting Δ_{VB} (meV)	Valley splitting (meV)
WSe_2	—	18.51	501.59	0	0	0
WSe_2/CrI_3	0	35.71 (36.52)	466.77 (466.99)	−0.40 (0.45)	0.03 (0.72)	−0.43 (−0.27)
	16.1	34.31 (34.33)	467.83 (468)	0.21 (0.23)	−1.43 (−1.51)	1.64 (1.74)
	23.4	36.57 (36.03)	433.48 (434.43)	1.26 (0.34)	−3.92 (−1.73)	5.18 (2.07)
	28.1	34.49 (33.96)	298.81 (298.65)	0.40 (0.18)	−3.29 (−3.43)	3.69 (3.61)

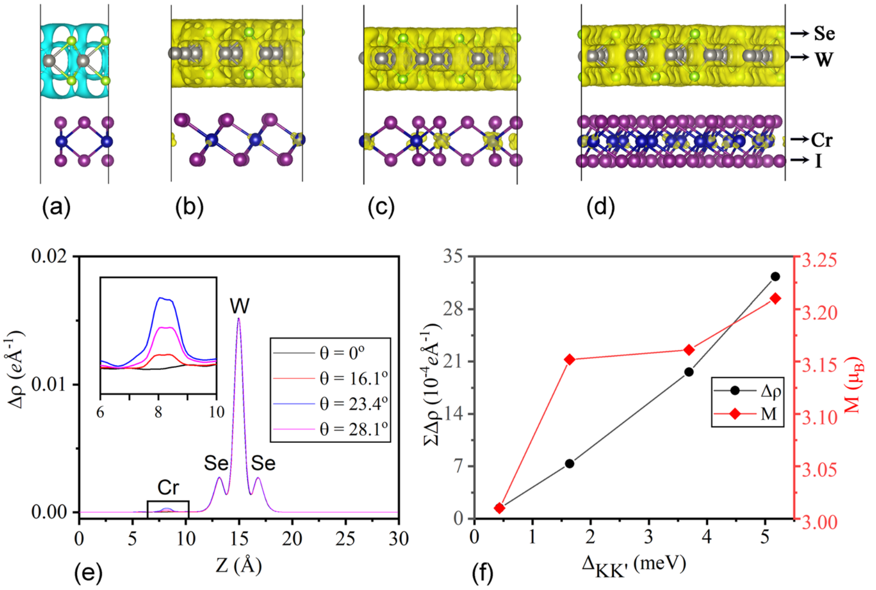

Fig. 5 Partial charge density differences of the VBM states between K and K′ for different θ. a $\theta = 0$, **b** 16.1, **c** 23.4, and **d** 28.1°. Isosurface is set at 5×10^{-5} e Å^{-3}. **e** Planar averaged partial charge density differences along z for states in (**a**–**d**). Inset is a zoom-in of the framed region at around $z = 8$ Å. **f** $\Sigma\Delta\rho$ and average magnetic moment of Cr atom M as functions of valley splitting $\Delta_{KK'}$.

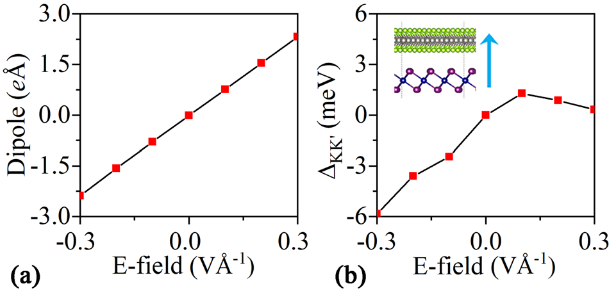

Fig. 6 Dipole moment and KK′ valley splitting as functions of applied E-field. a Dipole moment of the CrI_3/WSe_2 heterostructure. **b** Valley splitting at KK′ valleys. Inset in **b** shows the direction of the field.

field is also a direct consequence of MPE via an enhanced valley splitting.

In the discussion above, we have chosen a lattice parameter, e.g., that of WSe_2, to construct the supercells. It is desirable to consider the effect of strain. For this reason, Table 1 also shows the results when the lattice parameter is that of CrI_3. In line with above results, $\Delta_{KK'}$ for the Cr-HC configuration shows an increase with θ, e.g., 1.97 meV ($\theta = 16.1°$) < 3.69 meV ($\theta = 28.1°$).

There are two important consequences due to strain: (1) a direct-to-indirect gap crossover between $\theta = 0$ and 23.4°. To this end, recall that monolayer TMDs are direct gap semiconductors, in which both the VBM and conduction band minimum (CBM) are at the K (K′) valley of the Brillouin zone (see Fig. 3a)[3,5]. Previous experiments[43,44] and theory[35] also showed that the various physical properties of TMDs, including band gap and band edge positions in the Brillouin zone, can be tuned by applying an in-plane strain. In our calculations, the strain in WSe_2 changes from 5.4% (tensile) at $\theta = 0°$ to -3.25% (compressive) at $\theta = 23.4°$. In the former case, the CBM position is unchanged, but the VBM position moves from K (K′) to Γ. In the latter case, the VBM position is unchanged, but the CBM position moves to the Q (Q′) valley, which is about halfway between K (K′) and Γ, as shown in Fig. 3a. (2) The valley splitting for the Se-HC configuration vanishes at $\theta = 16.1°$. This is shown in Table 1 where for $\theta = 16.1°$, MAE = 0.27 meV Cr^{-1} is positive with an in-plane easy axis. The corresponding in-plane magnetic field can neither generate a Zeeman splitting nor lift the valley degeneracy. However, in this case, it is possible to obtain an easy axis component perpendicular to the 2D sheet by applying an external electric field (E-field). In the absence of the E-field, a small dipole of -0.016 eÅ is obtained, which is in line with a 0.0037 $e$$Cr^{-1}$ transfer from WSe_2 to CrI_3 by a Bader analysis[45]. Figure 6 shows the results for both dipole moment and KK′ valley splitting. A good linear relationship of the dipole moment with applied E-field is observed, and $\Delta_{KK'}$ can be tuned obviously by applying the external electric field. Taking E-field = -0.3 V Å^{-1} as an example, we find that MAE changes from 0.27 to -0.56 meV Cr^{-1}, and $\Delta_{KK'}$ changed from 0 to -5.84 meV. This magnetoelectric effect here is reminiscent of what has been observed in bilayer CrI_3[46], explaining the twist-induced enhancement of valley splitting in WSe_2/CrI_3 heterostructures.

The *k·p* model

To estimate the magnitude of the equivalent **B** and understand the Zeeman effect induced by CrI_3, we use a *k·p* model[34], in which the interaction energy is divided into spin and orbital contributions:

$$\mathbf{H}_B = g_0\mu_B\mathbf{B}\cdot\mathbf{S} + \mu_B\mathbf{B}\cdot\mathbf{L} \tag{9}$$

where $g_0 = 2$ is the Landé factor, $\mu_B = e\hbar/2m_0$ is the Bohr magneton, m_0 is the electron mass, $\mathbf{S} = \sigma/2$ is the spin operator with σ being the Pauli matrices, and $\mathbf{L}$ is the orbital angular momentum operator. As mentioned earlier, in the K (K′) valley the CBM state mainly consists of W d_{z^2} orbital with $L_Z = 0$, whereas the VBM state mainly consists of W $d_{x^2-y^2/xy}$ orbital with $L_Z = 2$. From the DFT computation, the spin projection around CB and VB band edges remains mostly out of plane with little in-plane tilting as shown in Supplementary Table 2. Therefore, the Rashba interaction is neglected in the present *k·p* model. The value $\sum_{i,j} VBM_i|\boldsymbol{H}_B|CBM_j$, where i and j run over the four levels near the Fermi level as shown in Fig. 3b, can be directly calculated via DFT, from which we deduce the equivalent **B**. For WSe_2/CrI_3 heterostructures with the Cr-HC configuration and WSe_2 lattice parameter, we obtain **B** = 2.1 T for $\theta = 0°$, 7.4 T for $\theta = 16.1°$, and 20.9 T for $\theta = 23.4°$. It shows that not only the magnetic field strength is sufficiently strong but also twisting can be an effective way to amplify the MPE at interfaces.

DISCUSSION

In summary, using first-principles calculation, we perform a systematic study on the structural stability, electronic and magnetic properties of 2D vdW WSe_2/CrI_3 heterostructures. We show that, compared to the non-twisted structure, the twisted ones are more stable, as evidenced by their higher interfacial binding energies. Our study also reveals an MAE of the heterostructures, which is controlled by strains of the CrI_3 layer. The MPE can be understood in terms of the charge density difference of the VBM states at K and K′. More importantly, in twisted heterostructures, there is an order of magnitude enhancement of K-K′ valley splitting, which can also be tuned by applying an external electric field. With the help of a *k·p* model, we determine the equivalent **B** field due to twisting as the origin of an enhanced MPE.

METHODS

First-principles calculations were performed using the Vienna ab initio simulation package (VASP) based on the density functional theory (DFT)[47]. We employed the Perdew–Burke–Ernzerhof (PBE)[48] functional, within the projector augmented wave (PAW)[49] approach, for exchange-correlation potential and energy. The plane-wave energy cutoff was set at 500 eV. vdW interactions between CrI_3 and WSe_2 were included by employing Grimme's semiempirical DFT-D3 scheme[50]. To avoid interaction between periodic images in the supercell approach, we used a vacuum space larger than 30 Å. The atomic structures were fully relaxed until the Feynman–Hellman force on each atom is less than 0.02 eV Å^{-1}. The electronic self-consistent convergence criterion was set at 10^{-7} eV. The K-point mesh[51] in the Brillouin zone was sampled with the density of 0.03 Å. To determine the magnetic anisotropy, the spin-orbit coupling (SOC) was included in our DFT calculations. In addition, we performed electronic structure calculations with GGA + U methods[52] described by Dudarev, in which the on-site Coulomb parameter U and the moderate exchange parameter J were set to 2.7 and 0.7 eV[53], respectively. The k-projection method[42] for interfaces modeled by supercells within the framework of the first-principles method was used to obtain the unfolded electronic band structures.

DATA AVAILABILITY

The data that support this work are available in the article and Supplementary Information file. Further raw data are available from the corresponding author (J.Z.) on reasonable request.

Received: 2 September 2021; Accepted: 23 January 2022;

REFERENCES

1. Novoselov, K. S. et al. Electric field effect in atomically thin carbon films. *Science* **306**, 666–669 (2004).
2. Manzeli, S., Ovchinnikov, D., Pasquier, D., Yazyev, O. V. & Kis, A. 2D transition metal dichalcogenides. *Nat. Rev. Mater.* **2**, 17033 (2017).

3. Splendiani, A. et al. Emerging photoluminescence in monolayer MoS_2. *Nano Lett.* **10**, 1271–1275 (2010).
4. Wang, M. et al. Robust memristors based on layered two-dimensional materials. *Nat. Electron.* **1**, 130–136 (2018).
5. Mak, K. F., Lee, C., Hone, J., Shan, J. & Heinz, T. F. Atomically thin MoS_2: a new direct-gap semiconductor. *Phys. Rev. Lett.* **105**, 136805 (2010).
6. Chen, S. et al. Origin of ultrafast growth of monolayer WSe_2 via chemical vapor deposition. *npj Comput. Mater.* **5**, 28 (2019).
7. Huang, B. et al. Layer-dependent ferromagnetism in a van der Waals crystal down to the monolayer limit. *Nature* **546**, 270 (2017).
8. Gong, C. & Zhang, X. Two-dimensional magnetic crystals and emergent heterostructure devices. *Science* **363**, 706 (2019).
9. Wilson, J. A. & Yoffe, A. D. The transition metal dichalcogenides discussion and interpretation of the observed optical, electrical and structural properties. *Adv. Phys.* **18**, 193–335 (1969).
10. Fang, H. et al. High-performance single layered WSe_2 p-FETs with chemically doped contacts. *Nano Lett.* **12**, 3788–3792 (2012).
11. Ross, J. S. et al. Electrically tunable excitonic light-emitting diodes based on monolayer WSe_2 p-n junctions. *Nat. Nanotechnol.* **9**, 268–272 (2014).
12. Mak, K. F. & Shan, J. Photonics and optoelectronics of 2D semiconductor transition metal dichalcogenides. *Nat. Photon* **10**, 216–226 (2016).
13. Burch, K. S., Mandrus, D. & Park, J. G. Magnetism in two-dimensional van der Waals materials. *Nature* **563**, 47–52 (2018).
14. Geim, A. K. & Grigorieva, I. V. Van der Waals heterostructures. *Nature* **499**, 419–425 (2013).
15. Deng, D. et al. Catalysis with two-dimensional materials and their heterostructures. *Nat. Nanotechnol.* **11**, 218–230 (2016).
16. Szendrő, M., Süle, P., Dobrik, G. & Tapasztó, L. Ultra-flat twisted superlattices in 2D heterostructures. *npj Comput. Mater.* **6**, 91 (2020).
17. Cao, Y. et al. Unconventional superconductivity in magic-angle graphene superlattices. *Nature* **556**, 43–50 (2018).
18. Wu, F., Lovorn, T., Tutuc, E., Martin, I. & MacDonald, A. H. Topological insulators in twisted transition metal dichalcogenide homobilayers. *Phys. Rev. Lett.* **122**, 086402 (2019).
19. Liao, M. et al. Twist angle-dependent conductivities across MoS_2/graphene heterojunctions. *Nat. Commun.* **9**, 4068 (2018).
20. Sierra, J. F., Fabian, J., Kawakami, R. K., Roche, S. & Valenzuela, S. O. Van der Waals heterostructures for spintronics and opto-spintronics. *Nat. Nanotechnol.* **16**, 856–868 (2021).
21. Xiao, D., Liu, G. B., Feng, W., Xu, X. & Yao, W. Coupled spin and valley physics in monolayers of MoS_2 and other group-VI dichalcogenides. *Phys. Rev. Lett.* **108**, 196802 (2012).
22. Li, Y. et al. Valley splitting and polarization by the Zeeman effect in monolayer $MoSe_2$. *Phys. Rev. Lett.* **113**, 266804 (2014).
23. Aivazian, G. et al. Magnetic control of valley pseudospin in monolayer WSe_2. *Nat. Phys.* **11**, 148–152 (2015).
24. Srivastava, A. et al. Valley Zeeman effect in elementary optical excitations of monolayer WSe_2. *Nat. Phys.* **11**, 141–147 (2015).
25. Qi, J., Li, X., Niu, Q. & Feng, J. Giant and tunable valley degeneracy splitting in $MoTe_2$. *Phys. Rev. B* **92**, 121403 (2015).
26. Zhao, C. et al. Enhanced valley splitting in monolayer WSe_2 due to magnetic exchange field. *Nat. Nanotechnol.* **12**, 757–762 (2017).
27. Lado, J. L. & Fernández-Rossier, J. On the origin of magnetic anisotropy in two dimensional CrI_3. *2D Mater.* **4**, 035002 (2017).
28. Zhong, D. et al. Layer-resolved magnetic proximity effect in van der Waals heterostructures. *Nat. Nanotechnol.* **15**, 187–191 (2020).
29. Zhong, D. et al. Van der Waals engineering of ferromagnetic semiconductor heterostructures for spin and valleytronics. *Sci. Adv.* **3**, 1–6 (2017).
30. Seyler, K. L. et al. Valley manipulation by optically tuning the magnetic proximity effect in WSe_2/CrI_3 heterostructures. *Nano Lett.* **18**, 3823–3828 (2018).
31. Zhang, Z., Ni, X., Huang, H., Hu, L. & Liu, F. Valley splitting in the van der Waals heterostructure WSe_2/CrI_3: the role of atom superposition. *Phys. Rev. B* **99**, 115441 (2019).
32. Hu, T. et al. Manipulation of valley pseudospin in WSe_2/CrI_3 heterostructures by the magnetic proximity effect. *Phys. Rev. B* **101**, 125401 (2020).
33. Zollner, K., Junior, P. E. F. & Fabian, J. Proximity exchange effects in $MoSe_2$ and WSe_2 heterostructures with CrI_3 twist angle, layer, and gate dependence. *Phys. Rev. B* **100**, 085128 (2019).
34. Wang, G. et al. Magneto-optics in transition metal diselenide monolayers. *2D Mater.* **2**, 034002 (2015).
35. Deng, S., Li, L. & Li, M. Stability of direct band gap under mechanical strains for monolayer MoS_2, $MoSe_2$, WS_2 and WSe_2. *Phys. E Low. Dimens. Syst. Nanostruct.* **101**, 44–49 (2018).
36. Wang, Y. et al. Strain-induced direct–indirect bandgap transition and phonon modulation in monolayer WS_2. *Nano Res.* **8**, 2562–2572 (2015).
37. Lee, C. et al. Frictional characteristics of atomically thin sheets. *Science* **328**, 76–80 (2010).
38. Zheng, F. et al. Tunable spin states in the two-dimensional magnet CrI_3. *Nanoscale* **10**, 14298–14303 (2018).
39. Medeiros, P. V. C., Stafström, S. & Björk, J. Effects of extrinsic and intrinsic perturbations on the electronic structure of graphene: retaining an effective primitive cell band structure by band unfolding. *Phys. Rev. B* **89**, 041407 (2014).
40. Medeiros, P. V. C., Tsirkin, S. S., Stafström, S. & Björk, J. Unfolding spinor wave functions and expectation values of general operators: introducing the unfolding-density operator. *Phys. Rev. B* **91**, 041116 (2015).
41. Ku, W., Berlijn, T. & Lee, C. C. Unfolding first-principles band structures. *Phys. Rev. Lett.* **104**, 216401 (2010).
42. Chen, M. & Weinert, M. Layer k-projection and unfolding electronic bands at interfaces. *Phys. Rev. B* **98**, 245421 (2018).
43. Aslan, O. B., Deng, M. & Heinz, T. F. Strain tuning of excitons in monolayer WSe_2. *Phys. Rev. B* **98**, 115308 (2018).
44. Park, K.-D. et al. Hybrid tip-enhanced nanospectroscopy and nanoimaging of monolayer WSe_2 with local strain control. *Nano Lett.* **16**, 2621–2627 (2016).
45. Henkelman, G., Arnaldsson, A. & Jónsson, H. A fast and robust algorithm for Bader decomposition of charge density. *Comput. Mater. Sci.* **36**, 354–360 (2006).
46. Jiang, S., Shan, J. & Mak, K. F. Electric-field switching of two-dimensional van der Waals magnets. *Nat. Mater.* **17**, 406–410 (2018).
47. Kresse, G. & Furthmiiller, J. Efficiency of ab-initio total energy calculations for metals and semiconductors using a plane-wave basis set. *Comput. Mater. Sci.* **6**, 15–50 (1996).
48. Perdew, J. P., Burke, K. & Ernzerhof, M. Generalized gradient approximation made simple. *Phys. Rev. Lett.* **77**, 3865 (1996).
49. Kresse, G. & Joubert, D. From ultrasoft pseudopotentials to the projector augmented-wave method. *Phys. Rev. B* **59**, 1758 (1999).
50. Grimme, S., Antony, J., Ehrlich, S. & Krieg, H. A consistent and accurate ab initio parametrization of density functional dispersion correction (DFT-D) for the 94 elements H-Pu. *J. Chem. Phys.* **132**, 154104 (2010).
51. Monkhorst, H. J. & Pack, J. D. Special points for Brillouin-zone integrations. *Phys. Rev. B* **13**, 5188 (1976).
52. Dudarev, S. L., Botton, G. A., Savrasov, S. Y., Humphreys, C. J. & Sutton, A. P. Electron-energy-loss spectra and the structural stability of nickel oxide: an LSDA + U study. *Phys. Rev. B* **57**, 1505 (1998).
53. Wang, R., Su, Y., Yang, G., Zhang, J. & Zhang, S. Bipolar doping by intrinsic defects and magnetic phase instability in monolayer CrI_3. *Chem. Mater.* **32**, 1545–1552 (2020).

ACKNOWLEDGEMENTS

Work in China was supported by the National Natural Science Foundation of China (12074235). S.Z. acknowledges the support by the U.S. Department of Energy (DOE) under Grant no. DESC0002623. C.S. also acknowledges support by the open research fund program of the state key laboratory of low dimensional quantum physics (KF202103).

AUTHOR CONTRIBUTIONS

J.Z. and S.Z. supervised the project. M.G. and H.W. designed and performed the DFT calculations. J.W. and C.S. developed the k·p model. M.G. wrote the manuscript. All authors discussed the results and reviewed the manuscript.

COMPETING INTERESTS

The authors declare no competing interests.

ADDITIONAL INFORMATION

Supplementary information The online version contains supplementary material available at https://doi.org/10.1038/s41524-022-00715-9.

Correspondence and requests for materials should be addressed to Junfeng Zhang or Shengbai Zhang.

Reprints and permission information is available at http://www.nature.com/reprints